# Dynamic response characteristics of CFRP/steel-cylinder confined rubber cement mortar based on cyclic impact loading

*R.-Z. Yang*[1] ✉ iD *, Y. Xu*[1] iD *, P.-Y. Chen*[2] iD

[1] *State Key Laboratory of Mining Response and Disaster Prevention and Control in Deep Coal Mines, Anhui University of Science and Technology, Huainan, China*

[2] *School of Civil Engineering and Architecture, Anhui University of Science and Technology, Huainan, China*

✉ *Rongzhouy @outlook.com*

**Abstract.** Rubber cement-based material is one of the important ways of utilizing waste rubber. Fatigue failure and impact failure are the most common failure forms of concrete structures, but the low stiffness and low strength of rubber cement-based materials do no allow them to be used in the main bearing structure. Therefore, the use of appropriate reinforcement materials and technical methods to effectively improve the yield stiffness, bearing capacity, ductility, and energy dissipation capacity of rubber cement-based materials can not be ignored. To explore the dynamic response characteristics of rubber cement mortar (RCM) with different confine conditions, the split Hopkinson pressure bar (SHPB) cyclic impact tests of four kinds of confined RCM were carried out. Firstly, the four different confine modes of RCM were designed by using the carbon fiber reinforced polymer (CFRP) sheet and steel cylinder. Then, the SHPB test system was used to carry out the amplitude-enhanced cyclic impact tests of RCM with different confine modes. Lastly, the dynamic mechanical behavior, energy behavior, dynamic damage, and failure modes of RCM with different confine modes were compared and analysed. The results show that the end faces and side of RCM were confined effectively by using the CFRP sheet and steel cylinder, which strengthened the structural resistance of RCM. However, with the simultaneous increase in impact load and impact times, stiffness degradation still occurred due to the cumulative effect of fatigue damage. The end friction constraint of the CFRP sheet and the passive confining pressure constraint of the CFRP sheet/steel cylinder significantly improved the energy dissipation capacity and impact resistance of RCM, controlled and delayed the transverse expansion deformation and crack development of RCM, and ensured the minimum damage of RCM structure. The purpose of this paper is to provide a reference for further promoting the resource utilization of waste rubber and the practical engineering application of rubber cement-based materials.

## 1. Introduction

Concrete material is commonly used in civil engineering and national defense engineering [1]. Fatigue failure and impact failure are the most common failure forms of concrete structures [1–3]. Under the action of vehicle load, wind load, seismic load, frequent explosion and impact loads, and other fatigue

loads, due to the evolution of internal microcracks and the development of damage, once the damage value exceeds the critical threshold, concrete will lose its bearing capacity, resulting in serious property losses and casualties [2]. Up to now, the problems of fatigue failure and dynamic damage of concrete materials are still prominent, especially in the aspect of dynamic fatigue failure. For this reason, many researchers have carried out a large number of experimental studies on the development of anti-fatigue concrete materials [4–5], the strengthening methods of concrete [6–7], and the impact resistance of concrete materials [8–9].

In the aspect of anti-fatigue concrete materials, a series of concrete materials such as fiber-reinforced concrete [5, 10], plastic concrete [11–12], and rubber concrete [13–14] have been developed, which improve the mechanical properties of ordinary concrete to some extent. However, some studies [13–18] have shown that rubber concrete materials have more outstanding properties in fatigue resistance [13–14], impact resistance [15–16], and explosion resistance [17–18]. As a result, rubber cement-based materials have attracted the attention of researchers, which makes them become the focus of the current research. Lv et al. [14] studied the fatigue behavior of self-compacting rubber lightweight aggregate concrete (SCRLC) under uniaxial compression. The results [14] show that the fatigue life and fatigue strain of SCRLC generally increases with the increase of rubber particle substitution rate, and the fatigue strain increases with the increase of cycle times. The fatigue performance of SCRLC is better than that of normal concrete. Yang et al. [15] carried out SHPB dynamic mechanical tests of rubber concrete under four loading modes. The results [15] show that rubber concrete shows ideal crack resistance and fatigue impact resistance. Yang et al. [17] carried out a field blasting test on the reinforced rubber concrete slab and proved that the reinforced rubber concrete slab is a practical explosion-proof structure, especially under the action of high energy explosion. Although rubber cement-based materials have a wide application prospect in earthquake resistance [19–20], roads [4, 21], and protective engineering [17–18], the low stiffness and strength of rubber cement-based materials are the key factors that it is difficult to be used as the main bearing structure.

In terms of strengthening methods of concrete, the use of appropriate reinforcement materials and techniques can significantly improve the yield stiffness, bearing capacity, ductility, and energy dissipation capacity of concrete materials. Carbon fiber reinforced polymer (CFRP) is a kind of composite material widely used in the field of civil engineering [22]. Because CFRP has superior mechanical properties to traditional materials, its application in the reinforcement and repair of concrete structures has been developed rapidly [22–32]. To comprehensively evaluate the strengthening effect of CFRP on concrete, researchers studied in detail the mechanical properties of CFRP-confined concrete from single to structure and from test to simulation. Wang et al. [29] carried out the SHPB cyclic impact compression test of CFRP-confined cement mortar, and the results showed that CFRP reduced the generation of cracks inside specimens, improved the ductility of specimens, and CFRP-confined cement mortar showed better impact resistance and energy absorption capacity. Xiong et al. [30] carried out an experimental study on the compressive performance of CFRP-confined concrete under a high strain rate. The results [30] show that CFRP can improve the strength and ductility of concrete. Li et al. [31] to clarify the bond-slip behavior of CFRP at the high loading rate (more than 800 mm/s), a new method for high loading rate impact test using an improved SHPB device was proposed, and the constitutive equation of dynamic bond-slip behavior of CFRP-concrete interface was established. Zhai et al. [32] proposed a method of using CFRP external bonding to repair prestressed concrete cylindrical tubes.

In addition to strengthening concrete with CFRP sheets, strengthening concrete with steel cylinder/tube with high stiffness is also a common reinforcement method in the field of stability of concrete structures, such as concrete-filled steel tubes [33–34]. However, there is little research on the dynamic fatigue impact of concrete strengthened with the steel cylinder. Tam et al. [33] studied the effect of the expansive agent on the axial compression behavior of recycled concrete-filled steel tubular short columns. It is found that due to the improvement of constraint conditions, the strength of expansive concrete-filled steel tubular columns is slightly higher than that of its benchmark concrete-filled steel tubular columns. Yang et al. [34] conducted an experimental study on the impact force, deformation, and energy absorption performance of a square steel tubular high-strength concrete column under transverse impact load by using a drop weight testing machine. The results [34] show that the square steel tubular high-strength concrete column has a strong impact resistance, which shows a higher impact platform value and a smaller deflection.

Based on the above research results, it can be known that although researchers have done a large number of experimental studies on rubber concrete and CFRP/steel cylinder confined concrete, they have never combined rubber concrete material with CFRP/steel cylinder reasonably and effectively. If the rubber concrete material can be effectively strengthened by using CFRP/steel cylinder, and the mode of "complementary advantages" between different materials can be formed, it plays a key role in fully improving the bearing capacity and fatigue performance of rubber concrete material. To solve this problem, this paper took RCM as the research object, used CFRP/steel cylinder to strengthen it in different confine methods, and the amplitude-enhanced cyclic impact tests with the help of the SHPB test system were

carried out. The dynamic response characteristics of CFRP/steel cylinder confined RCM were deeply explored and analysed from the aspects of dynamic mechanical behavior, energy characteristics, damage evolution, and failure states.

## 2. Methods

### 2.1. Test materials and specimen preparation

#### 2.1.1. Test raw materials

Cementitious material: 42.5 grade ordinary Portland cement (P.O 42.5); Mixed water: laboratory tap water; Fine aggregates: natural river sand with a density of 2600 kg/m$^3$ and a fineness modulus of 2.60 [35]; Rubber fine aggregates: waste tire rubber particles with a mesh of 20 and a density of 1120 kg/m$^3$ [35]; Confine materials: CFRP sheet and steel cylinder; CFRP sheet impregnated adhesive: epoxy resin and curing agent.

#### 2.1.2. Specimen preparation

The detailed process of specimen preparation with four different confine conditions in this experiment is shown in Fig. 1. In the first stage of specimen preparation: According to the standard JGJ/T 70-2009 [36], the specimens were removed after 24 hours of casting and molding, and the specimens after demoulding were placed in an environment with a temperature of (20 ± 2) °C and humidity greater than 90 % for 28 days. In the second stage of specimen preparation: Firstly, the unconfined impact specimen with a size of $\varPhi$ 50 mm × $h$ 25 mm was obtained after a series of the processing; Secondly, two kinds of impact specimens with different CFRP confines were prepared by using CFRP sheet impregnated adhesive to paste single-layer CFRP sheet on the upper, lower round end and side of the unconfined impact specimen; Finally, the passive confining pressure confine was carried out on the unconfined impact specimen with the help of high modulus steel cylinder. Combined with the preparation method, the impact specimens with four different confine conditions were obtained. In addition, the static uniaxial compression test of unconfined RCM specimens with a size of $\varPhi$ 50 mm × $h$ 100 mm was carried out by using WAW-2000 electro-hydraulic servo universal testing machine, and the static compression strength was about 15.45 MPa.
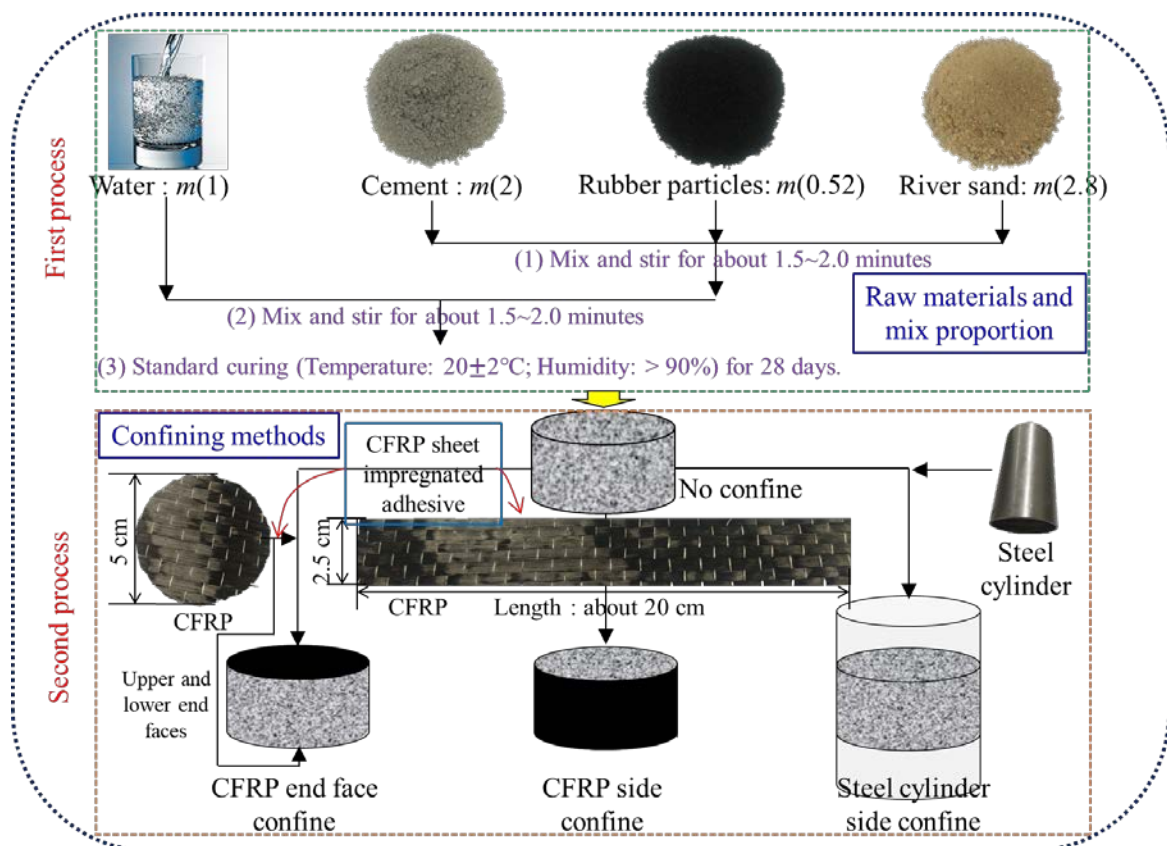


**Figure 1. The preparation process of the specimens with four different confine conditions.**

In this test, the physical and technical parameters of the CFRP sheet, CFRP sheet impregnated adhesive, and steel cylinder are shown in Table 1.

**Table 1. Physical and technical parameters of CFRP sheet, CFRP sheet impregnated adhesive, and steel cylinder.**

| CFRP sheet | | CFRP sheet impregnated adhesive | | Steel cylinder | |
|---|---|---|---|---|---|
| Strength grading | High strength level-2 | | | Material | High-alloy steel |
| Gram weight (g/m²) | 200 | Composition | ① Epoxy resin, ②curing agent | Height (mm) | 100.50 |
| Theoretical thickness (mm) | 0.111 | | | | |
| Tensile strength (MPa) | 3325 | | | Thickness (mm) | 1.96 |
| Elastic modulus (MPa) | 2.40 × 10⁵ | Mixed proportion | 2(①) : 1(②) | | |
| Elongation (%) | 1.74 | | | | |
| General component-Design value of tensile strength (MPa) | 2000 | Design value of shear strength (MPa) | 18 | Inner diameter (mm) | 51.67 |
| General component-Design value of elastic modulus (MPa) | 2.0 × 10⁵ | | | Density (g/cm³) | 7.85 |
| General component-Design value of strain resistant (%) | 1 | Solid content (%) | 99.6 | | |

## 2.2. SHPB system and test principle

SHPB system: this test used a variable cross-section SHPB test system with a diameter of 50 mm in the Impact Dynamics Laboratory of Anhui University of Science and Technology, as shown in Fig. 2. The bar material in the SHPB test system is alloy steel with a density of 7.8 g/cm³ and an elastic modulus of 210 GPa. The power system consists of high-pressure nitrogen, gas valve, launch chamber, impact bars, and automatic launcher. The data acquisition and processing system consisting of the resistance strain gauge, KD6009 strain amplifier, MDO3024 oscilloscope, and computer.

Test principle: the SHPB testing principle is based on the one-dimensional elastic stress wave hypothesis and the stress/strain uniformity hypothesis (two basic hypotheses) [37]. According to the strain signals collected by strain gauges on the incident bar and transmission bar, combined with one-dimensional stress wave theory [37] and cyclic impact deformation effect [15, 37–38], the equations for calculating strain rate, strain, and stress of cyclic impact specimens under the three-wave method can be derived:

$$\begin{cases} \varepsilon_{i+1} = \dfrac{C\int_0^t \left( \varepsilon_{I(i+1)} - \varepsilon_{R(i+1)} - \varepsilon_{T(i+1)} \right) \mathrm{d}t}{L_{S(i-1)} - \varepsilon_i L_{S(i-1)}} \\[4mm] \dot{\varepsilon}_{i+1} = \dfrac{C\left( \varepsilon_{I(i+1)} - \varepsilon_{R(i+1)} - \varepsilon_{T(i+1)} \right)}{L_{S(i-1)} - \varepsilon_i L_{S(i-1)}} \\[4mm] \sigma_{i+1} = \dfrac{2AE}{\pi D_{Si}^2}\left( \varepsilon_{I(i+1)} + \varepsilon_{R(i+1)} + \varepsilon_{T(i+1)} \right) \end{cases} \tag{1}$$

where, $\varepsilon_{i+1}$, $\dot{\varepsilon}_{i+1}$, and $\sigma_{i+1}$ are the compressive strain, the compressive strain rate, and the compressive stress of the specimen under the ($i$+1)-th cycle impact, respectively; $E$, $A$, and $C$ are the elastic modulus, the cross-sectional area, and the wave velocity of the compression bars, respectively; $\varepsilon_{I(i+1)}$, $\varepsilon_{R(i+1)}$, and $\varepsilon_{T(i+1)}$ are the incident strain, the reflection strain, and the transmission strain of the compression bars under the ($i$+1)-th cycle impact, respectively; $L_{Si}$ is the length of the specimen under the $i$-th cycle impact; $D_{Si}$ is the diameter of specimen under the $i$-th cycle impact.

The equations of the three-wave method were further simplified to that of the two-wave method:

$$\begin{cases} \varepsilon_{i+1} = \dfrac{2C\int_0^t \left(\varepsilon_{I(i+1)} - \varepsilon_{T(i+1)}\right)dt}{L_{S(i-1)} - \varepsilon_i L_{S(i-1)}} \\[4mm] \overset{\bullet}{\varepsilon}_{i+1} = \dfrac{2C\left(\varepsilon_{I(i+1)} - \varepsilon_{T(i+1)}\right)}{L_{S(i-1)} - \varepsilon_i L_{S(i-1)}} \\[4mm] \sigma_{i+1} = \dfrac{4AE}{\pi D_{Si}^2}\varepsilon_{T(i+1)} \end{cases} \tag{2}$$
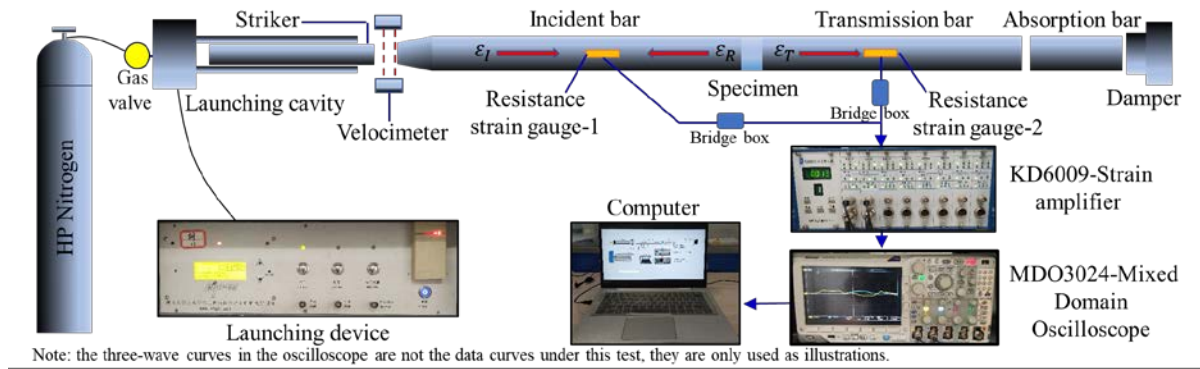
It should be noted that the diameter of the circular end face of the specimen changes very little in the process of cyclic impact. To facilitate the calculation of the stress of the specimen under the cyclic impact, it can be assumed that the diameter of the circular end face of the specimen remains unchanged in the process of cyclic impact, that is, the area of the circular end face is approximately constant [15]:

$$A_{S0} = \frac{\pi D_{S0}^2}{4} \approx A_{Si} = \frac{\pi D_{Si}^2}{4} \tag{3}$$

Therefore, Eq. (4) can be obtained from Eqs. (2)-(3):

$$\sigma_{i+1} = \frac{4AE}{\pi D_{Si}^2}\varepsilon_{T(i+1)} \approx \frac{4AE}{\pi D_{S0}^2}\varepsilon_{T(i+1)} \tag{4}$$

where, $A_{S0}$ and $D_{S0}$ are the initial cross-sectional area and the initial diameter of the specimen; $A_{Si}$ is the cross-sectional area of the specimen under the $i$-th cycle impact.



Note: the three-wave curves in the oscilloscope are not the data curves under this test, they are only used as illustrations.
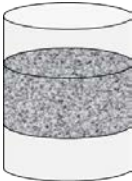
**Figure 2. Schematic diagram of SHPB dynamic test system.**

## 2.3. Test types and results

In the experiment, gradually increasing cyclic impact pressure was used to carry out cyclic impact tests on the specimens with four different confine conditions. The test types and test results are listed in Table 2.

**Table 2. Test types and test results of the specimens.**

| | Test types | Sample type | Impact pressure (MPa) | Number of cyclic impacts |
|---|---|---|---|---|
|  | No confine | No-C-1 | 0.2 | |
| | | No-C-2 | 0.3 | 3 |
| | | No-C-3 | 0.4 | |
|  | CFRP end face confine | CFRP-E-C-1 | 0.2 | |
| | | CFRP-E-C-2 | 0.3 | 4 |
| | | CFRP-E-C-3 | 0.4 | |
| | | CFRP-E-C-4 | 0.5 | |
|  | CFRP side confine | CFRP-S-C-1 | 0.2 | |
| | | CFRP-S-C-2 | 0.3 | 4 |
| | | CFRP-S-C-3 | 0.4 | |
| | | CFRP-S-C-4 | 0.5 | |
|  | Steel cylinder side confine | SC-S-C-1 | 0.2 | |
| | | SC-S-C-2 | 0.3 | |
| | | SC-S-C-3 | 0.4 | |
| | | SC-S-C-4 | 0.5 | 7 |
| | | SC-S-C-5 | 0.6 | |
| | | SC-S-C-6 | 0.7 | |
| | | SC-S-C-7 | 0.8 | |

# 3. Results and Discussion
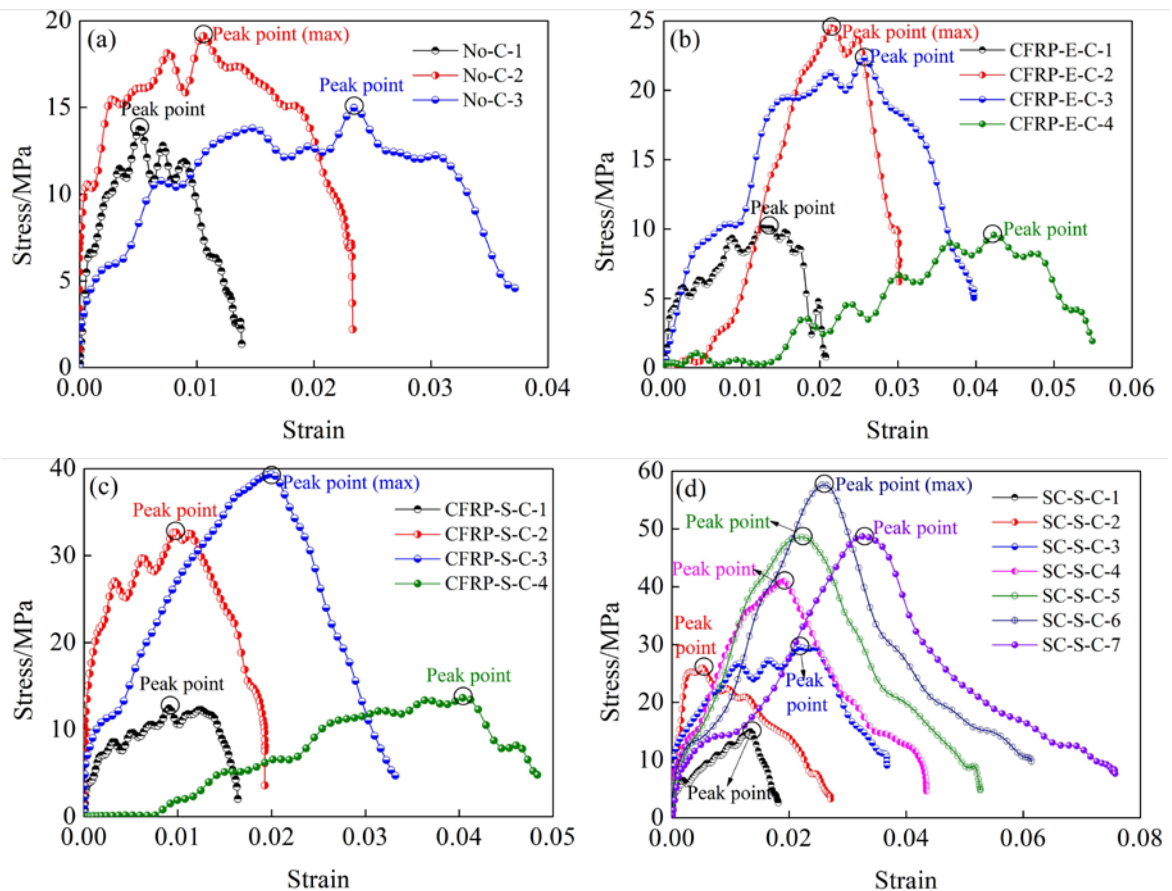
## 3.1. Stress-strain curves

The stress-strain curves of specimens with four different confines during the cyclic impact test are shown in Fig. 3. It can be seen from Fig. 3 that the stress-strain curves of specimens with four different confines showed similar behavior evolution characteristics to some extent, but there were also some obvious differences.

Similarly, the peak stress of specimens increased at first and then decreases with the increase of cyclic impact times, which reflected the evolution characteristic of "first cyclic hardening and then cyclic softening". The peak strain and ultimate strain of specimens increased with the synchronous increase of impact times and impact load, which showed obvious cyclic deformation ductility. The difference is that, compared with the specimen No-C, the impact resistance times of the specimens CFRP-E-C, CFRP-S-C, and SC-S-C were increased, especially the specimen SC-S-C showed better impact resistance, which showed that the end faces and side of the confined RCM specimen can improve its impact resistance. When the strength and stiffness of the confining material were larger, the specimen can withstand greater impact times and impact force. Many studies [3, 39–40] have shown that compared with normal cement-based materials, rubber cement-based materials have better impact resistance, but because of their low strength, rubber cement-based materials are effectively limited to a wider range of engineering applications. More importantly, under high-energy impact load, rubber cement-based materials will also lose structural resistance due to lower strength and then lose impact resistance. In other words, rubber cement-based materials will be seriously damaged due to low structural resistance under high-energy impact load, so that they are vulnerable to a single blow. As can be seen from Fig. 3, compared with specimen No-C, the maximum cyclic peak stress of specimens CFRP-E-C, CFRP-S-C, and SC-S-C increased by 28.34 %, 105.94 %, and 201.37 %, respectively. Thus it can be seen that the effective confinement on the end face and side of the RCM specimen can obviously improve the structural resistance of the material itself.
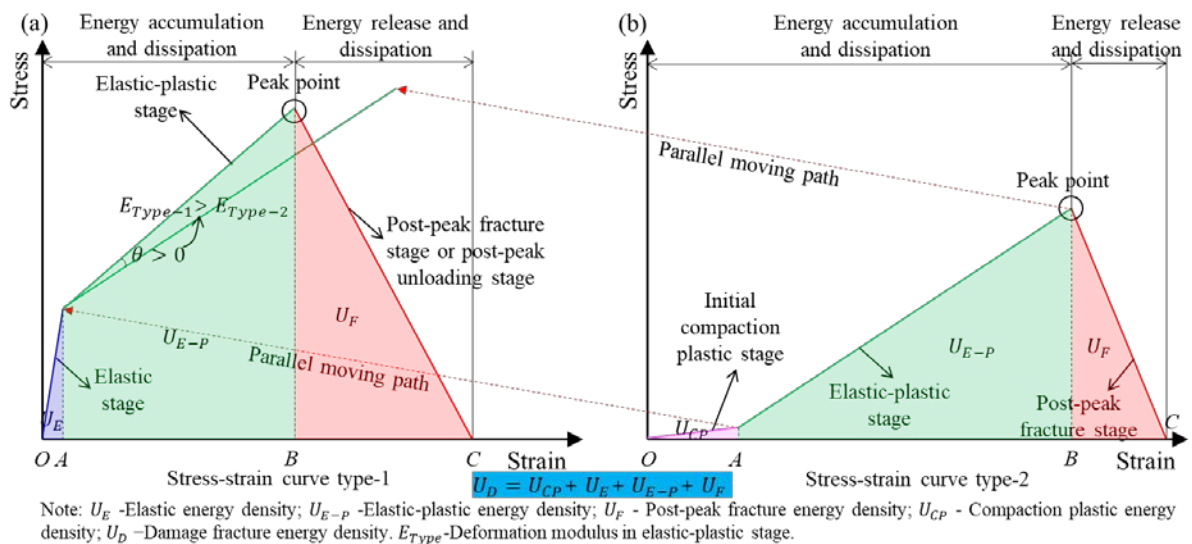
On the whole, it can be seen that the stress-strain curves of specimens under four different confines mainly showed two evolution types in the process of cyclic impact test. That is, stress-strain curve type-1 and stress-strain curve type-2 (Fig. 4). The main difference between stress-strain curve type-1 and stress-strain curve type-2 was that stress-strain curve type-1 mainly occurred in the first few impacts in the whole process of cyclic impact, while stress-strain curve type-1 mainly occurred in the last few impacts in the whole process of cyclic impact. The specific results are as follows: (1) at the initial stage of loading (*OA*), stress-strain curve type-1 had an obvious elastic stage, while stress-strain curve type-2 showed an obvious compaction stage; (2) in the later stage of loading (*BC*), stress-strain curve type-1 mainly occurred post-peak stress unloading or partial damage fracture, while stress-strain curve type-2 mainly occurred post-peak fracture damage; (3) in the elastic-plastic deformation stage (*AB*) of the stress-strain curves, it can be seen that the deformation modulus of the stress-strain curves decreased continuously with the synchronous

increase of impact times and impact load, especially reflected in the stress-strain curves of specimens CFRP-E-C and CFRP-S-C in the fourth impact (Fig. 3(b)-(c) and Fig. 4). According to fatigue damage mechanics, the essential reason leading to the behavior evolution characteristics of the above stress-strain curves and the difference between stress-strain curves is mainly due to the increase of structural damage and the degradation of stiffness due to the existence of damage cumulative effect or fatigue damage effect, which is mainly reflected in the generation of cracks, the development of cracks, and the formation of the fracture surface [2, 15, 41].

From the point of view of energy, the specimen mainly goes through three processes: energy accumulation, energy dissipation, and energy release in the process of cyclic impact, which is accompanied by four kinds of energy: compaction plastic energy, elastic energy, elastic-plastic energy, and post-peak fracture energy (see Fig. 4) [15]. Different energy densities of specimens during cyclic impact were defined, as shown in Fig. 4. The evolution characteristics of the energy density of the stress-strain curves are as follows: (1) In the *OA* stage, the elastic energy density was mainly reflected in the stress-strain curve type-1, and the compaction plastic energy density was mainly reflected in the stress-strain curve type-2, and the compaction plastic strain was significantly greater than the elastic strain. On this point, the specimen CFRP-E-C was more obvious than the specimen CFRP-S-C, which showed that the compaction hardening effect of the specimen CFRP-S-C was greater than that of the specimen CFRP-E-C. (2) In the *AB* stage, the elastic-plastic energy density of stress-strain curve type-1 was higher than that of stress-strain curve type-2, which indicated that the cyclic cumulative damage seriously weakened the structural bearing capacity of the specimen. Compared with specimen No-C, the elastic-plastic energy densities of specimens CFRP-E-C, CFRP-S-C, and SC-S-C were significantly increased, especially the elastic-plastic energy densities of specimens CFRP-S-C and SC-S-C were significantly increased under the side confine. (3) In the *BC* stage, the post-peak fracture energy density of stress-strain curve type-1 was higher than that of stress-strain curve type-2, and the post-peak residual bearing capacity of the specimens decreased significantly after the previous cyclic impacts. However, compared with the specimens with other confines, the post-peak fracture energy of the specimen SC-S-C decreased slightly in the last cycle, and still had larger post-peak fracture energy. To sum up, reasonable confine and reinforcement of RCM with effective confine materials can improve the structural fracture energy of RCM, which required higher external impact energy to cause structural damage to RCM after confine reinforcement, and then improved the impact resistance of RCM.



**Figure 3. Cyclic impact stress-strain curves of the specimens with four different confine conditions: (a) No-C; (b) CFRP-E-C; (c) CFRP-S-C; and (d) SC-S-C.**

Note: $U_E$ -Elastic energy density; $U_{E-P}$ -Elastic-plastic energy density; $U_F$ - Post-peak fracture energy density; $U_{CP}$ - Compaction plastic energy density; $U_D$ –Damage fracture energy density. $E_{Type}$ -Deformation modulus in elastic-plastic stage.

**Figure 4. Simplified types cyclic impact stress-strain curves of the specimens with four different confine conditions: (a) stress-strain curve type-1; and (b) stress-strain curve type-2.**
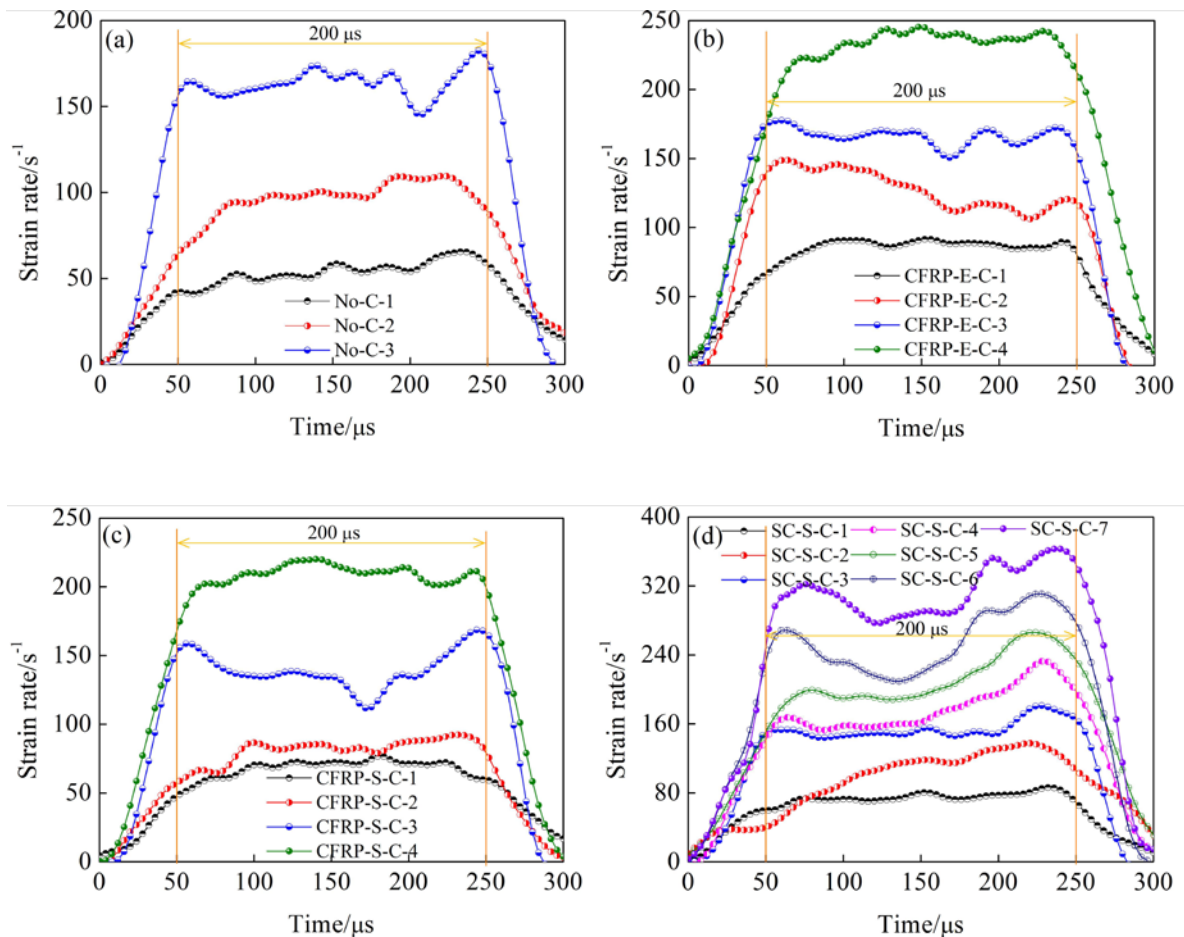
### 3.2. Strain rate-time curves and stress rate-time curves

The strain rate-time curves and stress rate-time curves of specimens with four different confine conditions during cyclic impact tests are shown in Fig. 5-6. It can be seen from Fig. 5-6 that the strain rate-time curves and stress rate-time curves of specimens with four different confines showed similar behavior evolution characteristics to some extent, but the behavior evolution characteristics of strain rate-time curves and stress rate-time curves were quite different.

#### 3.2.1. Strain rate-time curves

The observation and analysis of the evolution characteristics of the strain rate-time curves showed that the strain rate-time curves were approximately longitudinal axisymmetric, and its evolution characteristics became more obvious with the synchronous increase of impact times and impact load. The strain rate-time curves can be divided into three evolution stages: Strain rate growth stage, strain rate fluctuation stage, and strain rate attenuation stage [Fig. 5, Fig. 7 (a)]. The evolution characteristics of the strain rate-time curves are as follows: (1) In the strain rate growth stage (0 ~ 50 μs), the strain rate increased linearly at the initial stage of impact load, and the strain rate increased obviously with the synchronous increase of impact times and impact load, which led to a certain strain of the specimen. (2) In the strain rate fluctuation stage (50 ~ 250 μs), the strain rates of the specimens mainly showed the development trend of horizontal fluctuation, and the horizontal fluctuation of strain rate lasted for a relatively long time, reaching about 200 μs, resulting in a larger strain of the specimen, so that it exceeded the peak strain. Therefore, the loading process of approximately constant strain rate was the main stage leading to the damage of the specimen. (3) In the strain rate attenuation stage (250 ~ 300 μs), the strain rates of the specimens under the impact load in the later period decreased rapidly in a linear form mainly due to the unloading of the impact load, and the strain rate attenuation rate increased obviously with the synchronous increase of the impact times and the impact load. In the process of strain rate attenuation to 0, the strain continues to increase to the maximum.

**Figure 5. Cyclic impact strain rate-time curves of the specimens with four different confine conditions: (a) No-C; (b) CFRP-E-C; (c) CFRP-S-C; and (d) SC-S-C.**

### 3.2.2. Stress rate-time curves

For the stress rate-time curve, the evolution characteristics of its behavior are more complex, but on the whole, there are certain rules to follow. The stress rate-time curves as a whole showed five stages: initial fluctuation stability (*a-b*), positive abrupt change (*b-c-d*), medium-term fluctuation stability attenuation (*d-e-f*), negative abrupt change (*f-g-h*), and later fluctuation stability (*h-i*). The shapes of the stress rate-time curves were approximately central-symmetric, while the corresponding stress-time curves were approximately axisymmetric [Fig. 6, Fig. 7 (b)]. In general, the evolution characteristics of the above stress rate-time curves became more obvious with the synchronous increase of impact times and impact load, but the fluctuation amplitude and peak value of stress rate under the last impact decreased to some extent. Even zero value continued to appear in the initial stage, reflecting the obvious strain-softening phenomenon. According to the simplified stress rate-time curve, the specific evolution characteristics of the stress rate with time are as follows: (1) In the pre-peak stage (*OA*), the stress rate of the specimen was greater than zero, and the strain-softening effect was less than the strain-hardening effect, so the stress increased, and the stress rate reached the maximum at the positive abrupt change point *c*. As can be seen from Fig. 7 (b), when the stress increased to the point after *c*, the stress rate showed a downward trend of first fast and then slow under the strain rate fluctuates steadily, indicating that the specimen had slight structural damage in the *c-d-e* stage. In the *c-d-e* stage, as the stress rate decreased to 0, the corresponding stress increased to the maximum and reached the peak stress. (2) In the post-peak stage (*AB*), the stress rate of the specimen was less than zero, and the strain-softening effect was greater than the strain-hardening effect, so the stress decreased, and the stress rate reached the minimum at the negative abrupt change point *g*. As can be seen from Fig. 7 (b), when the stress decreased to the point before *g*, the stress rate showed a downward trend of first slow and then fast under the strain rate fluctuates steadily, indicating that the specimen had large structural damage in the *e-f-g* stage. Subsequently, the stress rate increased rapidly in the *g-h* stage, and then entered a fluctuating and stable state, which indicated that the specimen still had a certain residual bearing capacity after large damage in the post-peak *e-f-g* stage.
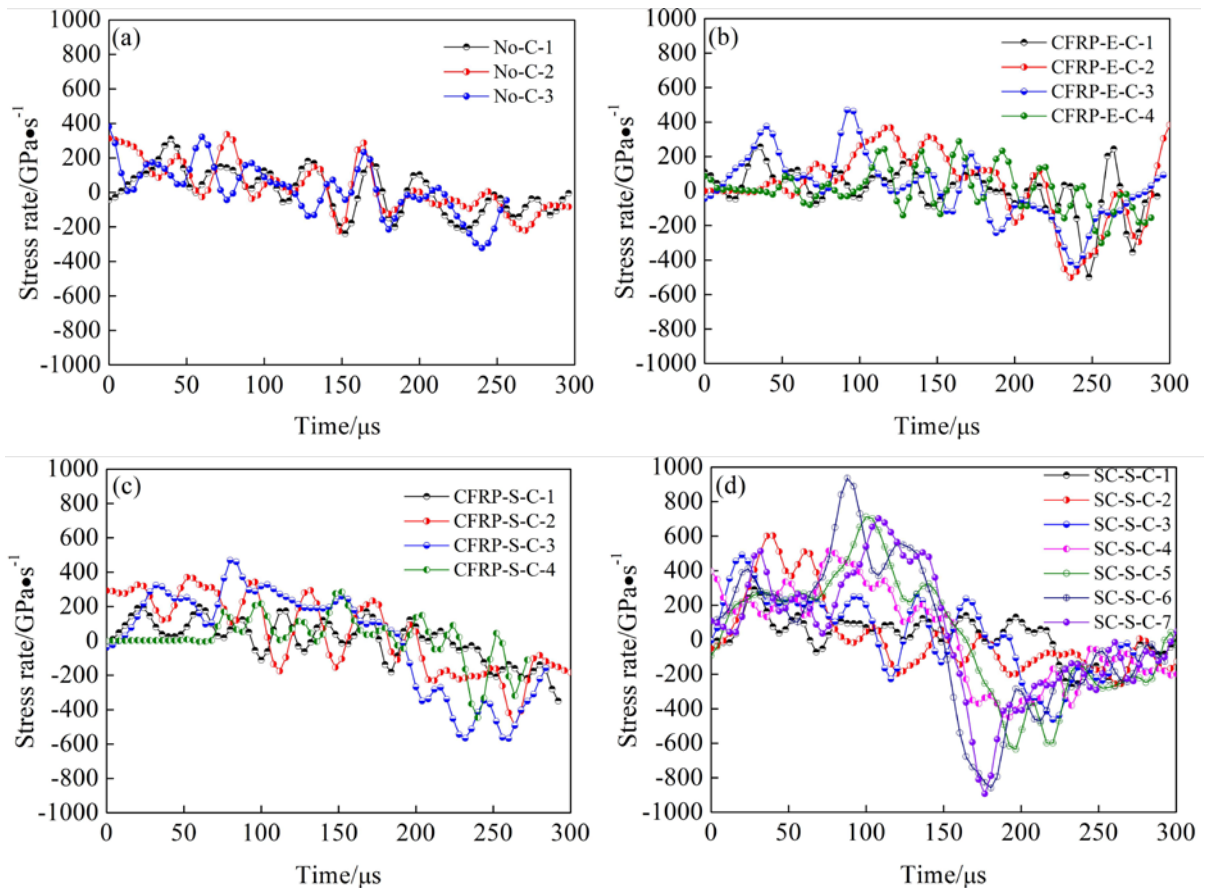
**Figure 6. Cyclic impact stress rate-time curves of rubber cement mortar specimens with four different confine conditions: (a) No-C; (b) CFRP-E-C; (c) CFRP-S-C; and (d) SC-S-C.**
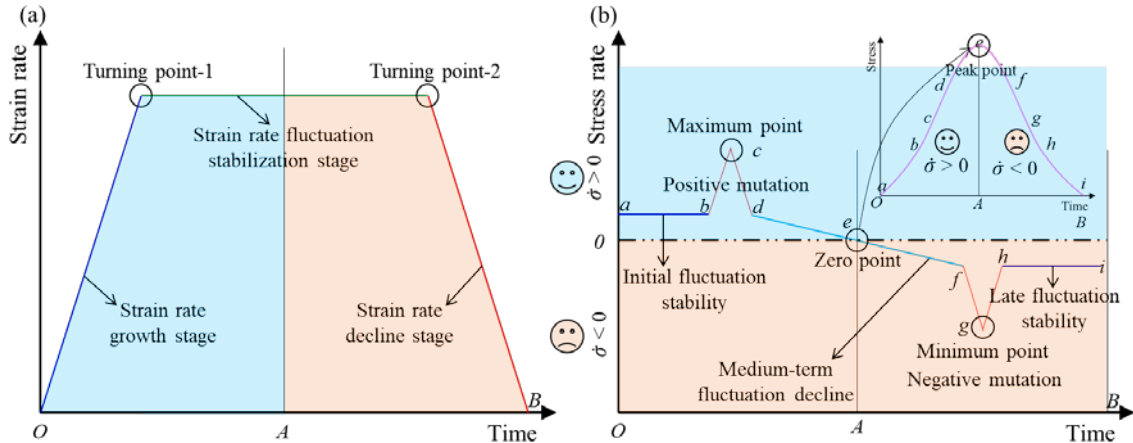


**Figure 7. Simplified behavior characteristics of (a) strain rate-time curve and (b) stress rate-time curve of the specimens with four different confine conditions under cyclic impact test.**

### 3.3. Energy evolution characteristics

#### 3.3.1. Energy in test and its calculation principle

Based on the one-dimensional stress wave theory, the incident energy, reflected energy, and transmitted energy in the SHPB cyclic impact testing process can be obtained from the incident strain, reflected strain, and transmitted strain in the bars, respectively. The specific calculation equations are as follows [42–43]:

$$W_{I,\text{Total}} = \sum_{i}^{n} W_{Ii} \rightarrow W_{Ii} = AEC \int_0^t \varepsilon_{Ii}^2 \mathrm{d}t \tag{5}$$

$$W_{R,\text{Total}} = \sum_{i}^{n} W_{Ri} \rightarrow W_{Ri} = AEC \int_0^t \varepsilon_{Ri}^2 \, dt \tag{6}$$

$$W_{T,\text{Total}} = \sum_{i}^{n} W_{Ti} \rightarrow W_{Ti} = AEC \int_0^t \varepsilon_{Ti}^2 \, dt \tag{7}$$

$$W_{D,\text{Total}} = \sum_{i}^{n} W_{Di} \rightarrow W_{Di} = -2AEC \int_0^t \varepsilon_{Ri} \varepsilon_{Ti} \, dt \tag{8}$$

where, $W_{I,\text{Total}}$, $W_{R,\text{Total}}$, $W_{T,\text{Total}}$, and $W_{D,\text{Total}}$ are the total incident energy, total reflection energy, total transmission energy, and total damage energy during the whole SHPB cycle impact test, respectively; $W_{Ii}$, $W_{Ri}$, $W_{Ti}$, and $W_{Di}$ are the incident energy, reflection energy, transmission energy, and damage energy under the $i$-th cycle impact, respectively.

The energy ratio can directly reflect the specific distribution and transformation of energy. To explore the evolution characteristics of energy under cyclic impact from the point of view of energy ratio, according to the above energy calculation method, the corresponding calculation equations of energy ratios are[43]:

$$\begin{cases} \eta_{R,\text{Total}} = \dfrac{W_{R,\text{Total}}}{W_{I,\text{Total}}}; \quad \eta_{Ri} = \dfrac{W_{Ri}}{W_{Ii}} \\[2ex] \eta_{T,\text{Total}} = \dfrac{W_{T,\text{Total}}}{W_{I,\text{Total}}}; \quad \eta_{Ti} = \dfrac{W_{Ti}}{W_{Ii}} \\[2ex] \eta_{D,\text{Total}} = \dfrac{W_{D,\text{Total}}}{W_{I,\text{Total}}}; \quad \eta_{Di} = \dfrac{W_{Di}}{W_{Ii}} \end{cases} \tag{9}$$

where, $\eta_{R,\text{Total}}$, $\eta_{T,\text{Total}}$, and $\eta_{D,\text{Total}}$ are the total reflection energy ratio, total transmission energy ratio, and total damage energy ratio during the whole SHPB cycle impact tests, respectively; $\eta_{Ri}$, $\eta_{Ti}$, and $\eta_{Di}$ are the reflection energy ratio, transmission energy ratio, and damage energy ratio under the $i$-th cyclic impact, respectively.

### 3.3.2. Energy and energy ratio

The relationship between the energy, energy ratio and confining conditions, impact times of the specimen under cyclic impact is shown in Fig. 8-9. Among them, Fig. 8 shows the relationship between the total energy, the total energy ratio and the confine conditions in the whole cyclic impact process, and Fig. 9 shows the relationship between the energy ratio and the impact times in the $i$-th impact process.

In terms of total energy, Fig. 8 (a) shows that the total reflection energy and total incident energy showed the same change with the change of confine conditions, and the total transmission energy and total damage energy showed the same change with the change of confine conditions. The details are as follows: ① Compared with specimen No-C, the total incident energies of specimens CFRP-E-C, CFRP-S-C, and SC-S-C can withstand complete failure under cyclic impact were significantly increased by 123.18 %, 99.60 %, and 535.84 %, respectively. ② Compared with specimen No-C, the total reflected energies dissipated by specimens CFRP-E-C, CFRP-S-C, and SC-S-C in complete failure under cyclic impact were increased by 162.68 %, 90.50 %, and 431.92 % respectively. ③ Compared with specimen No-C, the total transmission energies dissipated by specimens CFRP-E-C, CFRP-S-C, and SC-S-C during complete failure under cyclic impact were significantly increased by 26.95 %, 225.35 %, and 887.23 %, respectively. ④ Compared with specimen No-C, the total damage energies of specimens CFRP-E-C, CFRP-S-C, and SC-S-C can resist complete failure under cyclic impact were significantly increased by 56.07 %, 105.57 %, and 752.65 %, respectively. The above results confirm without a doubt that the CFRP and steel cylinder can significantly improve the energy dissipation capacity and impact resistance of RCM.

In terms of total energy ratio, Fig. 8 (b) shows that total reflection energy ratio > total damage energy ratio > total transmission energy ratio (0.02 ~ 0.06), which showed that total reflection energy and total damage energy were the main conversion objects of total incident energy, but it was undeniable that total reflection energy was the most important dissipation mode of total incident energy. At the same time, as can be seen from Fig. 8 (b), with the change of confine conditions, the total reflection energy ratio, total

damage energy ratio, and total transmission energy ratio showed a trend of "first increase then decrease", "first decrease then increase", and "first decrease then increase", respectively, and the total reflection energy ratio and total damage energy ratio were transversely axisymmetric to each other. The details are as follows: ① Total reflection energy ratio: CFRP-E-C > No-C > CFRP-S-C > SC-S-C; ② Total transmission energy ratio: CFRP-E-C < No-C < SC-S-C < CFRP-S-C; ③ Total damage energy ratio: CFRP-E-C < No-C < CFRP-S-C < SC-S-C. The above phenomena show that: ① The end-face restraint reinforcement of RCM with CFRP sheet leads to the increase of the total reflection energy ratio and then leads to the decrease of both the total transmission energy ratio and the total damage energy ratio. The main reason for this phenomenon is that the wave impedance of the CFRP sheet is lower than that of RCM, which further leads to a more mismatch between the wave impedance of CFRP-E-C and SHPB. ② The side restraint reinforcement of RCM with CFRP sheet and steel cylinder leads to the decrease of the total reflection energy ratio, which leads to the increase of the total transmission energy ratio and the total damage energy ratio. The main reason for this phenomenon is that the restrained reinforcement of CFRP sheet and steel cylinder effectively delays the development of cracks in RCM and ensures the minimization of structural damage.
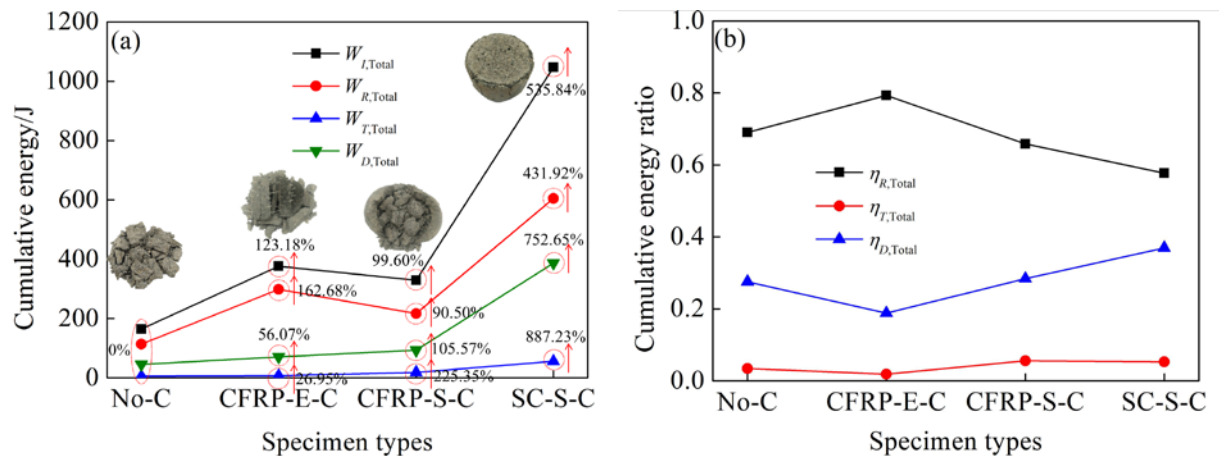


**Figure 8. Relationship between (a) cumulative total energy,
(b) cumulative total energy ratio and the confine conditions.**

Similarly, in terms of energy ratio, Fig. 9 shows that reflection energy ratio > damage energy ratio > transmission energy ratio, which showed that reflection energy and damage energy were the main conversion objects of incident energy. But it was undeniable that reflection energy was the most important way to dissipate incident energy. At the same time, as can be seen from Fig. 9, on the whole, with the increase of impact times, the reflection energy ratio, damage energy ratio, and transmission energy ratio showed the trend of "first decreasing and then increasing", "first increasing then decreasing", and "first increasing then decreasing", respectively, and the reflection energy ratio and damage energy ratio were transversely axisymmetric to each other. The details are as follows: ① The reason for the larger reflection energy ratio/lower damage energy ratio/lower transmission energy ratio under the first impact is that the initial specimen structure is in a compactible state, and the incomplete dense structure promotes the reflection of stress waves. ② The reason why the reflection energy ratio is larger/the damage energy ratio is smaller/the transmission energy ratio is smaller under the last impact is that the specimen structure is in a loose state due to the damage accumulation effect under the cyclic impact, and the loose structure also promotes the reflection of stress waves. ③ In addition to the first and last impact, in the whole intermediate impact process of cyclic impact, the reason for the smaller reflection energy ratio/larger damage energy ratio/larger transmission energy ratio is that the specimen structure promotes the compaction of the structure due to the first impact or the compaction effect of the previous times, suppresses the reflection of the stress wave and promotes the transmission of the stress wave. For the above results, CFRP-E-C, CFRP-S-C, and SC-S-C are more significant than No-C.
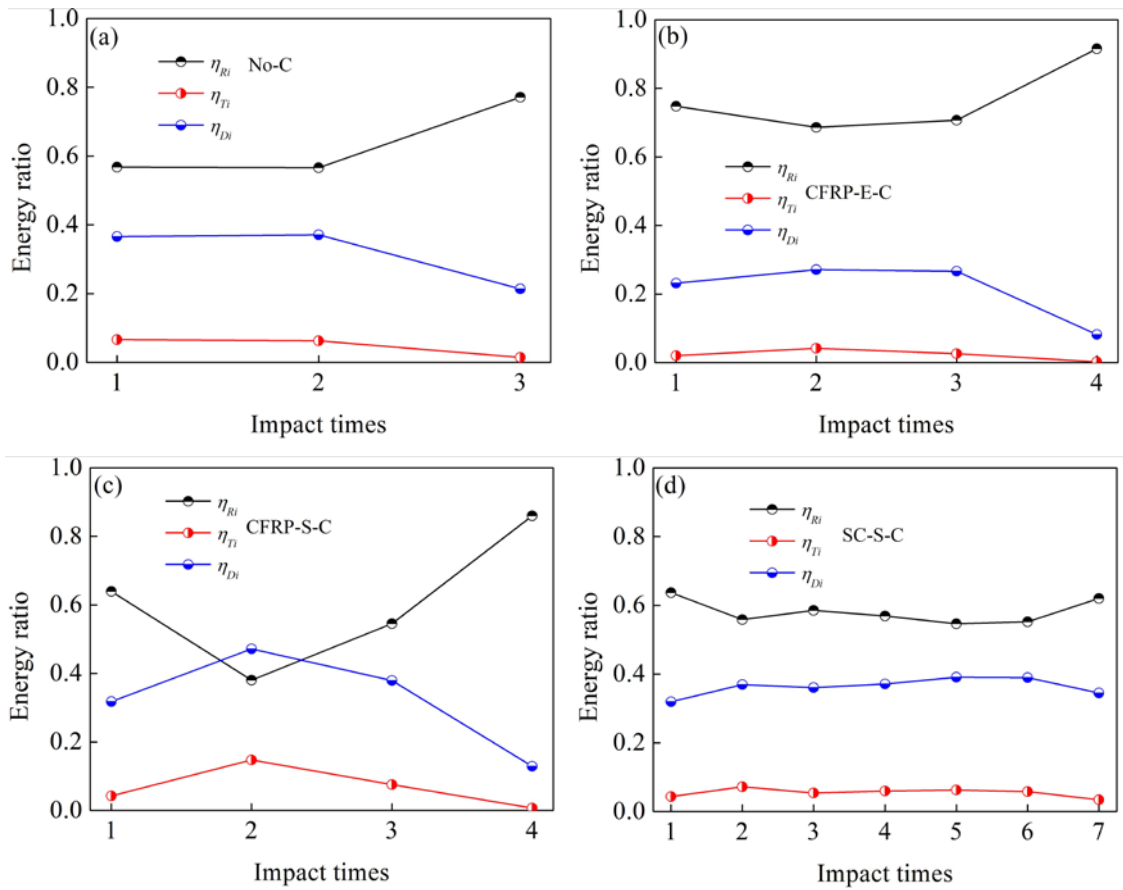
**Figure 9. Relationship between energy ratio and impact times:**
**(a) No-C; (b) CFRP-E-C; (c) CFRP-S-C; and (d) SC-S-C.**

### 3.4. Definition of damage variable and characteristics of damage evolution

#### 3.4.1. Definition of damage variable

To effectively evaluate the effects of four confine conditions on the impact fatigue damage of RCM, and to explore the evolution characteristics of impact fatigue damage of RCM. In this paper, the damage variables were defined from three aspects: peak stress, ultimate strain, and damage energy. The specific calculation equations are as follows:

$$D_{C-\text{peak stress}} = \sum_{i}^{n} \frac{\sigma_{\text{peak},i}}{\sigma_{\text{peak,Total}}} \tag{10}$$

$$D_{C-\text{ulimate strain}} = \sum_{i}^{n} \frac{\varepsilon_{\text{ult},i}}{\varepsilon_{\text{ult,Total}}} \tag{11}$$

$$D_{C-\text{damage energy}} = \sum_{i}^{n} \frac{W_{Di}}{W_{D,\text{Total}}} = \sum_{i}^{n} \frac{U_{Di}}{U_{D,\text{Total}}} \tag{12}$$

where, $D_{C-\text{peak stress}}$, $D_{C-\text{ulimate strain}}$, and $D_{C-\text{damage energy}}$ are the damage variables defined by the specimen in terms of peak stress, ultimate strain, and damage energy, respectively; $\sigma_{\text{peak},i}$ and $\sigma_{\text{peak,Total}}$ are the peak stress of the specimen in the $i$-th cycle impact and the cumulative peak stress of the specimen in the whole cycle impact process, respectively; $U_{Di}$ and $U_{D,\text{Total}}$ are the damage energy density of the specimen under the $i$-th cycle impact and the damage energy density of the specimen in the whole SHPB cycle impact test process, respectively.

### 3.4.2. Evolution characteristics of impact damage

It can be seen from Fig. 10 that the damage evolution characteristics of peak stress, ultimate strain, and damage energy were basically the same, that was, the values of damage variables increased with the increase of impact times, which showed that peak stress, ultimate strain, and damage energy can effectively characterize the fatigue damage characteristics of specimens in the process of cyclic impact. Fig. 10 shows that the characteristics of damage evolution were different with different confine conditions, and the damage growth rates of specimens CFRP-E-C, CFRP-S-C, and SC-S-C were lower than that of specimen No-C, which confirmed the fact that the restraint and reinforcement of CFRP sheet and steel cylinder can significantly reduce the damage growth rate. Especially with the confine of steel cylinder, the damage growth rate of RCM was the slowest, which stabilized the structure of RCM to a large extent and significantly weakened the cyclic impact fatigue damage effect. It can also be found that there was little difference in damage growth rate between CFRP-E-C and CFRP-S-C, which indicated that the restraining and strengthening effect of CFRP sheet on the end and side of RCM had a similar effect on the damage evolution characteristics of RCM under incremental cyclic impact.
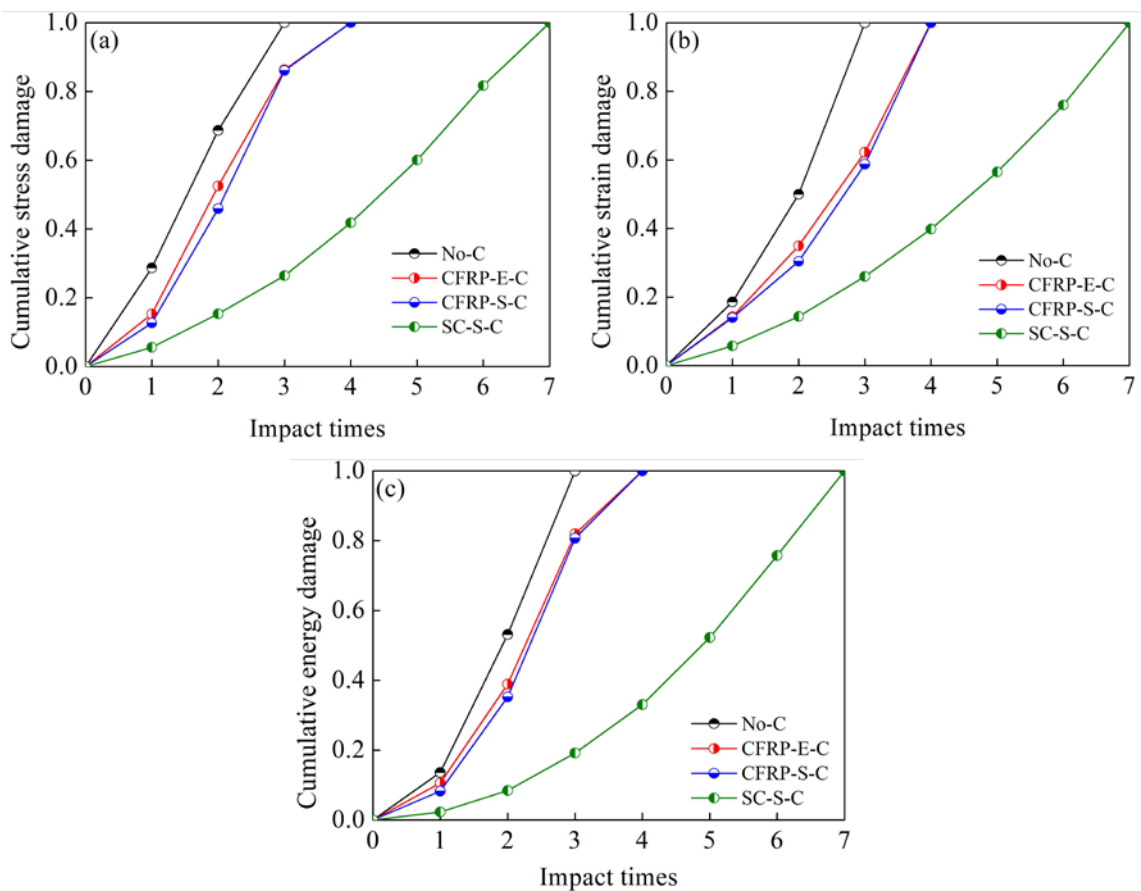


**Figure 10. Relationship between (a) stress damage,
(b) strain damage, and (c) energy damage and impact times.**

Fig. 11 shows the differences among the three damage variables established in terms of peak stress, ultimate strain, and damage energy. It can be seen from Fig. 11 that there was a great difference among the three damage variables of specimens No-C, CFRP-E-C, and CFRP-S-C, while the difference among the three damage variables of specimen SC-S-C was small, and it is not difficult to see that the difference between the three damage variables was relatively stable. Specifically, there were some similarities and differences among stress damage, strain damage, and energy damage of RCM with four confine conditions: ① The stress damage was basically above the strain damage and energy damage, which indicated that the stress damage was larger than the strain damage and energy damage in the evolution process. ② There was an intersection point *I* between strain damage and energy damage. In the stage before the intersection point *I*, the strain damage was above the energy damage, while in the stage after the intersection point *I*, the strain damage was below the energy damage or the strain damage basically coincides with the energy damage. Interestingly, for this phenomenon, there was a high similarity between specimens CFRP-E-C and CFRP-S-C, which fully showed that the restraint and strengthening effect of CFRP sheet on the end and side of RCM had a similar effect on the damage evolution of RCM under incremental cyclic impact.

To sum up, the three damage variables established from the three aspects of peak stress, ultimate strain, and damage energy can effectively characterize the impact fatigue damage evolution of RCM under the four confine conditions. However, from the difference among stress damage, strain damage, and energy damage, it is recommended to use stress damage to characterize the impact fatigue damage evolution of materials. The reason is that in the same cyclic impact state, the stress damage value is higher than strain damage and energy damage, so stress damage can play an effective role in warning the structural damage of RCM.
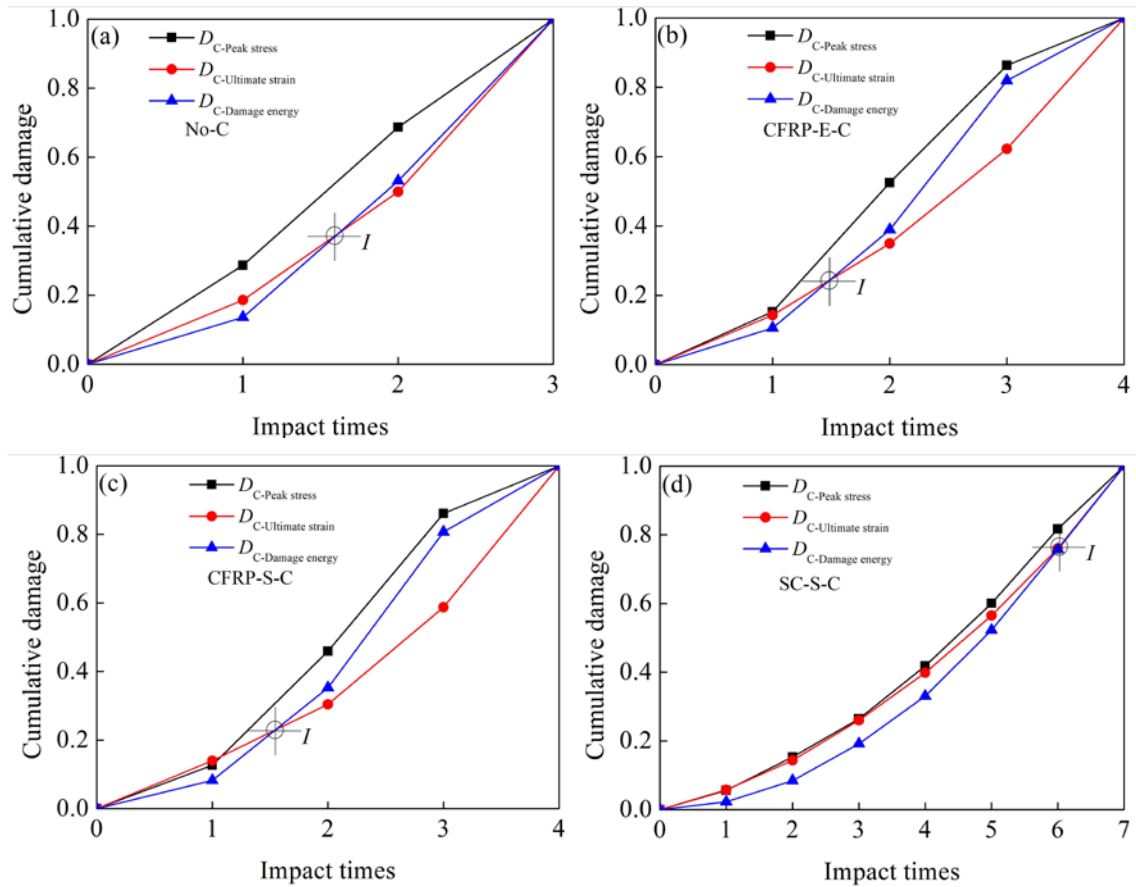


**Figure 11. Comparison of stress damage, strain damage, and energy damage of specimens with four different confine conditions: (a) No-C; (b) CFRP-E-C; (c) CFRP-S-C; and (d) SC-S-C.**

### 3.5. Failure states

The failure states of material specimens of different structures under impact load can reflect the dynamic damage modes, the mechanisms of fracture damage, and the mechanisms of structural crack resistance to a certain extent. As can be seen from Fig. 12, it is obvious that the cyclic impact damage process and failure states of RCM with four kinds of confines were quite different.

Fig. 12 (a) shows that a single fine crack clearly visible to the naked eye appeared in the side local area of the specimen No-C under the first cycle impact, and under the subsequent second cycle impact, the fine crack in this side area expanded into a coarse crack with larger crack width, and at the same time, the number of cracks increased. Under the third cycle impact, specimen No-C was completely damaged due to the excessive damage of the structural skeleton, which showed the compression failure of a transverse/radial free expansion. From this analysis, it can be seen that the mechanism of fracture damage is mainly due to the radial expansion deformation effect of specimen No-C under axial impact compression, and tensile cracks will appear in specimen No-C when the radial expansion deformation is greater than the ultimate tensile strain of specimen No-C. With the synchronous increase of impact times and impact pressure, the number and width of tensile cracks in specimen No-C must increase significantly. Finally, the specimen No-C is completely damaged under the combined action of axial compression and transverse tension.

Fig. 12 (b) shows that the specimen CFRP-E-C was seriously damaged under the third cycle impact, which was mainly reflected in the transverse tensile fracture of the end face and the expansion and spalling of the side. Under the fourth cyclic impact, the specimen CFRP-E-C mainly occurred along the fiber

direction until it is completely damaged, which generally showed the transverse fracture released by the friction confine of the end faces. Different from the specimen No-C, the structural crack resistance mechanism of specimen CFRP-E-C mainly lies in the synergistic effect of CFRP sheet and RCM, that was, the CFRP sheet of the end faces can play a certain role of buffer and radial restraint reinforcement of the end faces, and the transverse expansion deformation of the RCM matrix is restrained by the friction resistance effect of the end faces, which effectively improves the dynamic fatigue performance of the RCM.

Fig. 12 (c) shows that the specimen CFRP-S-C was also seriously damaged under the third cycle impact, which was mainly reflected in the damage behavior of the expansion and fracture of the CFRP sheet and the edge matrix. Under the fourth cyclic impact, the CFRP sheet of the specimen CFRP-S-C was broken into two halves and the intermediate matrix was completely damaged, which showed the transverse explosion fracture under the instantaneous release of confining pressure. The same as specimen CFRP-E-C, the crack resistance mechanism of specimen CFRP-S-C was mainly due to the synergistic effect of CFRP sheet and RCM. But the difference is that the side CFRP sheet can only play a certain role in radial restraint reinforcement, and the passive confining pressure effect restricts the transverse expansion deformation of the RCM matrix and effectively improves the dynamic fatigue performance of RCM.

Fig. 12 (d) and Fig. 13 show that the damage states of specimen SC-S-C under the first and second cyclic impacts were the same as that of specimen No-C. However, in the process of subsequent impact load, the passive confining pressure effect occurs due to the interaction between the RCM and the steel cylinder due to the transverse expansion deformation of RCM. The passive confining pressure exerted by the steel cylinder makes the development of the crack further controlled. With the synchronous increase of impact times and impact pressure, there were still more fine cracks in other parts of the specimen SC-S-C due to structural deformation. Finally, the specimen SC-S-C was damaged in the compound form of the matrix covered with fine cracks, side coarse cracks, and edge circumferential fracture, which generally showed the internal circumferential fracture which can not be released by the confining pressure. In terms of fracture damage and structural crack resistance mechanism, the fracture damage mechanism of specimen SC-S-C before the interaction between RCM and steel cylinder was the same as that of specimen No-C, and the structural crack resistance mechanism of specimen SC-S-C after the interaction between RCM and steel cylinder was the same as that of specimen CFRP-S-C. It is worth mentioning that the damage degree of RCM with the confine of the steel cylinder was obviously less than that of RCM with the confine of the CFRP sheet, and the specimen SC-S-C maintained a relatively complete shape, showing better dynamic fatigue resistance.
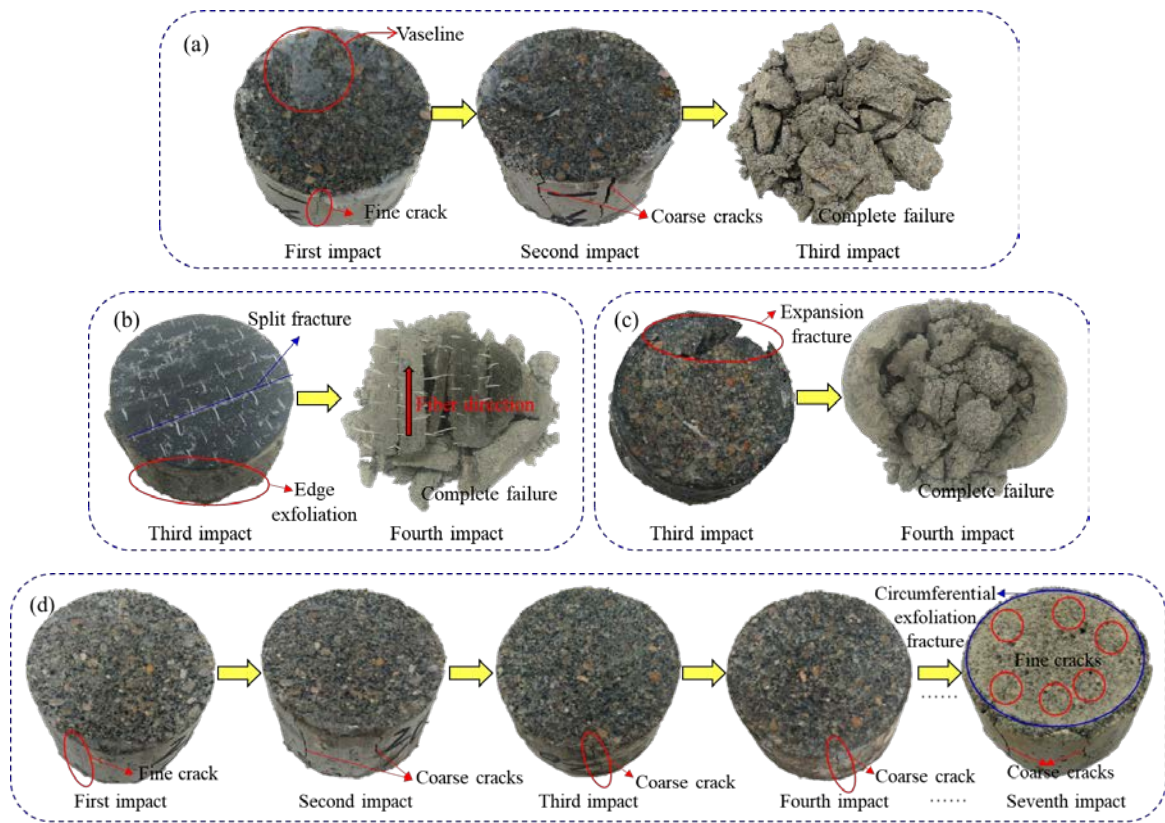


Note: To facilitate the observation of the fine cracks on the end face of the specimen, the picture of the specimen under the seventh impact was taken after the Vaseline on the surface of the specimen was dried, so the color of the specimen under the seventh impact is different from that of the previous impact specimens.

**Figure 12. Cyclic impact failure states of specimens with four different confine conditions: (a) No-C; (b) CFRP-E-C; (c) CFRP-S-C; and (d) SC-S-C.**
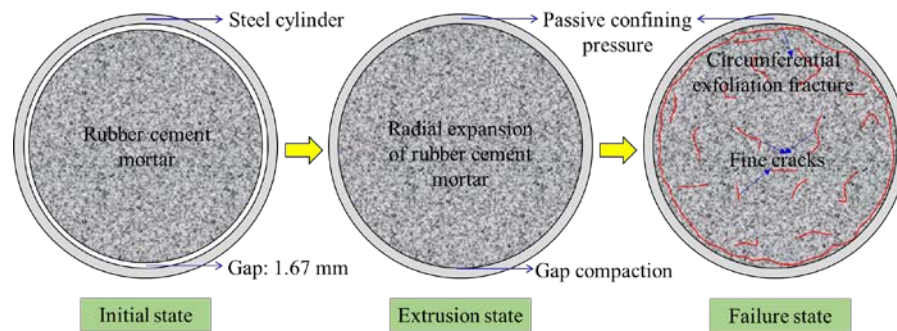
**Figure 13. Mechanism of dynamic fatigue fracture failure of specimen SC-S-C.**

To sum up, the structural crack resistance mechanism of confined RCM under cyclic impact load can be analysed from two aspects of material performance and confined structure mode. The details are as follows: (1) Compared with normal cement mortar, RCM itself has better impact resistance because of cushioning energy dissipation and plastic deformation [16]. (2) A "rigid-flexible combination" structure mode was formed under the rigid confines of the CFRP sheet and steel cylinder. The structure mode can play the role of "internal flexible energy consumption + external rigid confine = work along both lines" under cyclic impact load, and the effect of rigid-flexible joint crack resistance was formed.

# 4. Conclusions

In this paper, the amplitude-enhanced SHPB cyclic impact tests of four kinds of confined RCM were carried out, and the dynamic mechanical behavior, energy behavior, dynamic fatigue damage, and failure modes of RCM with the four confine conditions were compared and analysed. The following conclusions were drawn:

1. Compared with specimen No-C, the maximum cyclic peak stresses of specimens CFRP-E-C, CFRP-S-C, and SC-S-C were increased by 28.34 %, 105.94 %, and 201.37 %, respectively. It can be seen that the effective restraint on the end face and side of the RCM specimen obviously improved the structural resistance and structural damage fracture energy of the material itself. However, with the synchronous increase of impact load and impact times, stiffness degradation still occurred due to the cumulative effect of fatigue damage.

2. The shape of the strain rate-time curve was approximately longitudinal axial symmetry, showing three stages of growth, fluctuation stability, and attenuation, while the shape of the stress rate-time curve was approximately central symmetry, showing five stages of initial fluctuation stability, positive abrupt change, medium-term fluctuation stability attenuation, negative abrupt change, and late fluctuation stability. The above evolution characteristics became more obvious with the synchronous increase of impact times and impact load, but the fluctuation amplitude of the stress rate under the last impact decreased, which reflected the obvious strain-softening phenomenon.

3. Compared with specimen No-C, the total damage energies of specimens CFRP-E-C, CFRP-S-C, and SC-S-C increased by 56.07 %, 105.57 %, and 752.65 %, respectively, when the specimens were completely damaged in the process of cyclic impact, which fully proved that the confinement of CFRP and steel cylinder significantly improved the energy dissipation ability of RCM. The restrained reinforcement of CFRP sheet and steel cylinder effectively delays the development of cracks in RCM and ensures the minimization of structural damage.

4. With the increase of impact times, the reflected energy ratio, damage energy ratio, and transmission energy ratio showed a changing trend of "decreasing first and then increasing", "increasing first and then decreasing", and "increasing first and then decreasing", respectively. The reflected energy ratio and damage energy ratio showed a transverse axisymmetry state among each other. The three damage variables established from the three aspects of peak stress, ultimate strain, and damage energy can effectively characterize the impact fatigue damage evolution of RCM under the four confine conditions.

5. The failure modes of RCM with different confine modes were different. It was undeniable that RCM formed a "rigid-flexible combination" structure mode under the rigid confines of the CFRP sheet and steel cylinder. This structure mode can play the role of "internal flexible energy consumption + external rigid confine = work along both lines" under cyclic impact load, and the effect of rigid-flexible joint crack resistance was formed, which effectively improved the anti-fatigue impact performance of RCM.

## References

1. Zhang, S., Kong, X., Fang, Q., Chen, L., Wang, Y. Numerical prediction of dynamic failure in concrete targets subjected to projectile impact by a modified Kong-Fang material model. International Journal of Impact Engineering. 2020. 144. 103633. DOI: 10.1016/j.ijimpeng.2020.103633

2. Zhang, Q., Wang, L. Investigation of stress level on fatigue performance of plain concrete based on energy dissipation method. Construction and Building Materials. 2021. 269. 121287. DOI: 10.1016/j.conbuildmat.2020.121287

3. Assaggaf, R.A., Ali, M.R., Al-Dulaijan, S.U., Maslehuddin, M. Properties of concrete with untreated and treated crumb rubber-A review. Journal of Materials Research and Technology. 2021. 11. Pp. 1753–1798. DOI: 10.1016/j.jmrt.2021.02.019

4. Alsaif, A., Garcia, R., Figueiredo, F.P., Neocleous, K., Christofe, A., Guadagnini, M., Pilakoutas, K. Fatigue performance of flexible steel fibre reinforced rubberised concrete pavements. Engineering Structures. 2019. 193. Pp. 170–183. DOI: 10.1016/j.engstruct.2019.05.040

5. Ríos, J.D., Cifuentes, H., Blasón, S., López-Aenlle, M., Martínez-De La Concha, A. Flexural fatigue behaviour of a heated ultra-high-performance fibre-reinforced concrete. Construction and Building Materials. 2021. 276. 122209. DOI: 10.1016/j.conbuildmat.2020.122209

6. Al-Rousan, R.Z. Integration of CFRP strips as an internal shear reinforcement in reinforced concrete beams exposed to elevated temperature. Case Studies in Construction Materials. 2021. 14. e00508. DOI: 10.1016/j.cscm.2021.e00508

7. Zaiter, A., Lau, T.L. Experimental study of jacket height and reinforcement effects on seismic retrofitting of concrete columns. Structures. 2021. 31. Pp. 1084–1095. DOI: 10.1016/j.istruc.2021.02.020

8. Kheyroddin, A., Arshadi, H., Ahadi, M.R., Taban, G., Kioumarsi, M. The impact resistance of Fiber-Reinforced concrete with polypropylene fibers and GFRP wrapping. Materials Today: Proceedings. 2021. 45(6). Pp. 5433–5438. DOI: 10.1016/j.matpr.2021.02.116

9. Mezzal, S.K., Al-Azzawi, Z., Najim, K.B. Effect of discarded steel fibers on impact resistance, flexural toughness and fracture energy of high-strength self-compacting concrete exposed to elevated temperatures. Fire Safety Journal. 2021. 121. 103271. DOI: 10.1016/j.firesaf.2020.103271

10. Gao, D., Gu, Z., Zhu, H., Huang, Y. Fatigue behavior assessment for steel fiber reinforced concrete beams through experiment and Fatigue Prediction Model. Structures. 2020. 27. Pp. 1105–1117. DOI: 10.1016/j.istruc.2020.07.028

11. Adnan, H.M., Dawood, A.O. Recycling of plastic box waste in the concrete mixture as a percentage of fine aggregate, Construction and Building Materials. 2021. 284. 122666. DOI: 10.1016/j.conbuildmat.2021.122666

12. Carlesso, D.M., Cavalaro, S., de la Fuente, A. Flexural fatigue of pre-cracked plastic fibre reinforced concrete: Experimental study and numerical modeling. Cement and Concrete Composites. 2021. 115. 103850. DOI: 10.1016/j.cemconcomp.2020.103850

13. Hernández-Olivares, F., Barluenga, G., Parga-Landa, B., Bollati, M., Witoszek, B. Fatigue behaviour of recycled tyre rubber-filled concrete and its implications in the design of rigid pavements. Construction and Building Materials. 2007. 21 (10). Pp. 1918–1927. DOI: 10.1016/j.conbuildmat.2006.06.030

14. Lv, J., Zhou, T., Du, Q., Li, K. Experimental and analytical study on uniaxial compressive fatigue behavior of self-compacting rubber lightweight aggregate concrete. Construction and Building Materials. 2020. 237. 117623. DOI: 10.1016/j.conbuildmat.2019.117623

15. Yang, R., Xu, Y., Chen, P., Wang, J. Experimental study on dynamic mechanics and energy evolution of rubber concrete under cyclic impact loading and dynamic splitting tension. Construction and Building Materials. 2020. 262. 120071. DOI: 10.1016/j.conbuildmat.2020.120071

16. Pham, T.M., Chen, W., Khan, A.M., Hao, H., Elchalakani, M., Tran, T.M. Dynamic compressive properties of lightweight rubberized concrete. Construction and Building Materials. 2020. 238. 117705. DOI: 10.1016/j.conbuildmat.2019.117705

17. Yang, F., Feng, W., Liu, F., Jing, L., Yuan, B., Chen, D. Experimental and numerical study of rubber concrete slabs with steel reinforcement under close-in blast loading. Construction and Building Materials. 2019. 198. Pp. 423–436. DOI: 10.1016/j.conbuildmat.2018.11.248

18. Feng, W., Chen, B., Yang, F., Liu, F., Li, L., Jing, L., Li, H. Numerical study on blast responses of rubberized concrete slabs using the Karagozian and Case concrete model. Journal of Building Engineering. 2021. 33. 101610. DOI: 10.1016/j.jobe.2020.101610

19. Khan, I., Shahzada, K., Bibi, T., Ahmed, A., Ullah, H. Seismic performance evaluation of crumb rubber concrete frame structure using shake table test. Structures. 2021. 30. Pp. 41–49. DOI: 10.1016/j.istruc.2021.01.003

20. Youssf, O., ElGawady, M.A., Mills, J.E. Experimental investigation of crumb rubber concrete columns under seismic loading. Structures. 2015. 3. Pp. 13–27. DOI: 10.1016/j.istruc.2015.02.005

21. Pacheco-Torres, R., Cerro-Prada, E., Escolano, F., Varela, F. Fatigue performance of waste rubber concrete for rigid road pavements. Construction and Building Materials. 2018. 176. Pp. 539–548. DOI: 10.1016/j.conbuildmat.2018.05.030

22. Yazdani, S., Asadollahi, S., Shoaei, P., Dehestani, M. Failure stages in post-tensioned reinforced self-consolidating concrete slab strengthened with CFRP layers. Engineering Failure Analysis. 2021. 122. 105219. DOI: 10.1016/j.engfailanal.2021.105219

23. Al-Rousan, R. Impact of elevated temperature on the shear behavior of strengthened RC beams. Magazine of Civil Engineering. 2022. 110 (2). Article No. 11002. DOI: 10.34910/MCE.110.2

24. Jahami, A., Temsah, Y., Khatib, J., Baalbaki, O., Kenai, S. The behavior of CFRP strengthened RC beams subjected to blast loading. Magazine of Civil Engineering. 2021. 103 (3). Article No. 10309. DOI: 10.34910/MCE.103.9

25. Al-Rousan, R. Impact of elevated temperature on the behavior of strengthened RC beams with CFRP. Magazine of Civil Engineering. 2021. 106 (6). Article No. 10612. DOI: 10.34910/MCE.106.12

26. Al-Rousan, R. Behavior of CFRP strengthened columns damaged by thermal shock. Magazine of Civil Engineering. 2020. 97(5). Article No. 9708. DOI: 10.18720/MCE.97.8

27. Barham, W.S., Obaidat, Y.t., Alkhatatbeh, H.A. Behavior of heat damaged reinforced recycled aggregate concrete beams repaired with NSM-CFRP strips. Magazine of Civil Engineering. 2022. 111 (3). Article No. 11106. DOI: 10.34910/MCE.111.6

28. Zhang, X., Shi, Y., Li, Z.-X. Experimental study on the tensile behavior of unidirectional and plain weave CFRP laminates under different strain rates. Composites Part B: Engineering. 2019. 164. Pp. 524–536. DOI: 10.1016/j.compositesb.2019.01.067

29. Wang, J., Xu, Y., Yang, R., Zheng, Q., Ni, X. Dynamic mechanic and energy properties of cement mortar with CFRP confines. Journal of Building Materials. 2022. 25 (04). Pp. 344–352. DOI: 10.3969/j.issn.1007-9629.2022.04.003

30. Xiong, B., Demartino, C., Xiao, Y. High-strain rate compressive behavior of CFRP confined concrete: Large diameter SHPB tests. Construction and Building Materials. 2019. 201. Pp. 484–501. DOI: 10.1016/j.conbuildmat.2018.12.144

31. Li, G., Tan, K.H., Fung, T.C. Experimental study on CFRP-concrete dynamic debonding behaviour. Engineering Structures. 2020. 206. 110055. DOI: 10.1016/j.engstruct.2019.110055

32. Zhai, K., Fang, H., Guo, C., Fu, B., Ni, P., Ma, H., He, H., Wang, F. Mechanical properties of CFRP-strengthened prestressed concrete cylinder pipe based on multi-field coupling. Thin-Walled Structures. 2021. 162. 107629. DOI: 10.1016/j.tws.2021.107629

33. Tam, V.W.Y., Tao, Z., Evangelista, A. Performance of recycled aggregate concrete filled steel tubular (RACFST) stub columns with expansive agent. Construction and Building Materials. 2021. 272. 121627. DOI: 10.1016/j.conbuildmat.2020.121627

34. Yang, X., Yang, H., Zhang, S. Transverse impact behavior of high-strength concrete filled normal-/high-strength square steel tube columns. International Journal of Impact Engineering. 2020. 139. 103512. DOI: 10.1016/j.ijimpeng.2020.103512

35. Xu, Y., Yang, R. Dynamic mechanics and damage evolution characteristics of rubber cement mortar under different curing humidity levels. Journal of Materials in Civil Engineering. 2020. 32 (10). DOI: 10.1061/(ASCE)MT.1943-5533.0003351

36. JGJ/T 70-2009, Standard for test method of basic properties of construction mortar, China Architecture & Building Press, Beijing China. 2009.

37. Lu, F.Y., Chen, R., Lin, Y.L., Zhao, P.D., Zhang, D. Hopkinson bar techniques, Beijing: Science Press. 2013. ISBN: 978-7-03-038434-8.

38. Dai, B., Shan, Q.W., Chen, Y., Luo, X.Y. Mechanical and energy dissipation characteristics of granite under cyclic impact loading. Journal of Central South University. 2022. 29(01). Pp. 116–128. DOI: 10.1007/s11771-022-4897-9

39. He, L., Cai, H., Huang, Y., Ma, Y., Van Den Bergh, W., Gaspar, L., Valentin, J., Vasiliev, Y.E., Kowalski, K.J., Zhang, J. Research on the properties of rubber concrete containing surface-modified rubber powders. Journal of Building Engineering. 2021. 35. DOI: 10.1016/j.jobe.2020.101991

40. Feng, W., Liu, F., Yang, F., Jing, L., Li, L., Li, H., Chen, L. Compressive behaviour and fragment size distribution model for failure mode prediction of rubber concrete under impact loads. Construction and Building Materials. 2021. 273. 101991. DOI: 10.1016/j.conbuildmat.2020.121767

41. Feng, L., Chen, X., Zhang, J., Yuan, J., Dong, W. Fatigue behavior and prediction model of self-compacting concrete under constant amplitude load and incremental amplitude load. International Journal of Fatigue. 2021. 145. 106107. DOI: 10.1016/j.ijfatigue.2020.106107

42. Gong, F.Q., Zhong, W.H., Gao, M.Z., Si, X.F., Wu, W.X. Dynamic characteristics of high stressed red sandstone subjected to unloading and impact loads. Journal of Central South University. 2022. 29 (02). Pp. 596–610. DOI: 10.1007/s11771-022-4944-6

43. Shu, R., Yin, T., Li, X., Yin, Z., Tang, L. Effect of thermal treatment on energy dissipation of granite under cyclic impact loading. Transactions of Nonferrous Metals Society of China. 2019. 29 (2). Pp. 385–396. DOI: 10.1016/S1003-6326(19)64948-4

*Information about authors:*

**Rong-Zhou Yang,** *PhD*
*ORCID: https://orcid.org/0000-0002-0126-2446*
*E-mail: Rongzhouy@outlook.com*

**Ying Xu,** *PhD*
*ORCID: https://orcid.org/0000-0001-8438-3130*
*E-mail: yxu@aust.edu.cn*

**Pei-Yuan Chen,** *PhD*
*ORCID: https://orcid.org/0000-0002-5538-617X*
*E-mail: peiyuan29@126.com*